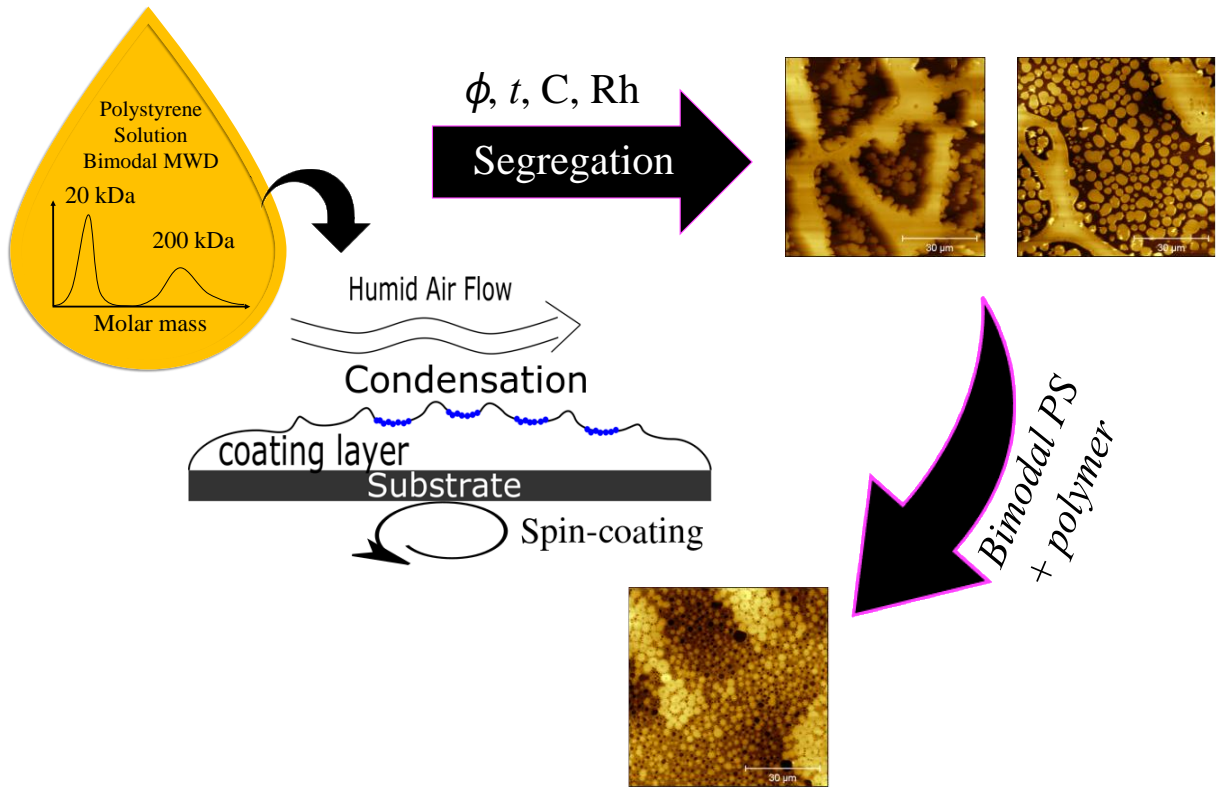


1 TOC



2

3

4 **Exploiting the interplay between bi-modal molecular weight distribution in polystyrene**  
5 **and humidity to induce self-assembly of biomimetic micropillars/honeycomb morphology**  
6 **in thin polymer film**

7 Authors: Maciej Łojkowski<sup>1,\*</sup>, Adrian Chlanda<sup>1,2</sup>, Emilia Choińska<sup>1</sup>, Wojciech  
8 Swieszkowski<sup>1,\*</sup>.

9

10 Affiliation:

11 1. Faculty of Material Sciences and Engineering, Warsaw University of Technology,  
12 Wołoska 141, 02-507 Warsaw, Poland

13 2. Department of Chemical Synthesis and Flake Graphene, Łukasiewicz Research  
14 Network - Institute of Microelectronics and Photonics, Aleja Lotników 32/46, 02-  
15 668 Warsaw, Poland.

16 **Abstract**

17 Segregation of polymer chains of different molecular weights is a well-known process. A  
18 traditional experimental approach of studying phase segregation of thin films composed of  
19 polymer blends with identical chemical compositions but different molecular weights, was  
20 focused on functionalization of chemical group or modification of end-group. In this study  
21 however, a different approach was proposed, in which polystyrene with a bimodal molecular  
22 weight distribution but no additional chemical modification was implemented in order to  
23 examine and analyze its phase segregation. It was found that by choosing right molecular  
24 weight distribution it is possible to obtain controlled phase separation at short time interval and  
25 at microscale. By doing this, we have presented an easy, fast, effective and fully controlled  
26 method of obtaining biomimetic micropillar/honeycomb morphologies. In addition, the  
27 evaporation rate during spin-coating and the viscosity of a solution with a bimodal molecular  
28 weight distribution was studied.

29 **Keywords**

30 self-assembly; polymer thin films; bimodal molecular weight distribution; polystyrene; spin-  
31 coating; pillars; honeycomb;

32

33 **Introduction**

34 Biomimetic complex morphologies comprising micropillars have gained attention due to  
35 their wide range of possible applications, for example, their special wetting properties (1,2),  
36 application in studying of biofilm formation (3) or controlling stem cells differentiation (4).

37 Two widespread methods which allow creation of a broad range of structures of polymer thin  
38 films (PTFs) are spin-coating (5) and breath figures (6). These methods were applied for  
39 manufacturing organic ferroelectric switches (7), light emitting devices (8), sensors (9,10),  
40 drug delivery systems (11,12), biologically active surfaces (13,14), functional nanostructured  
41 surfaces (15,16), and membranes (17). Both these processes rely heavily on the interaction  
42 dynamics between the solvent, the polymer and the vapors in the vicinity of the surface. In the  
43 case of spin-coating, a droplet of a mixture of a solvent and one or two polymers is dropped  
44 onto the substrate and subsequently the substrate is rotated very quickly to cover it uniformly  
45 with the liquid film of the solution. As a result, the solvent evaporates thus a solvent and  
46 temperature quench occurs. The change of the solvent volume and temperature often leads to  
47 unintentional or intentional liquid-liquid phase separation. (18) It has been argued that such  
48 phase separation often starts in the early stages of spinning. (18,19) The further spinning of the  
49 solution leads to gel formation which eventually slows down the diffusion inside the film. As a  
50 result, the occurring morphology becomes frozen in time before reaching an equilibrium. The  
51 time necessary for the morphology to stop evolving depended on such factors as the solvent  
52 evaporation rate, solution viscosity or spinning rate. (20,21) In case of the second  
53 aforementioned technique, the breath figures appear on the surface of the liquid film when the

54 humid air flow accelerates the evaporation rate. Successively, the temperature decreases which  
55 results in nucleation and growth of water droplets. These droplets create the regular a  
56 honeycomb array of cavities in the film. After most of the solvent had evaporated the  
57 temperature increases to that of the surroundings, the droplets evaporate leaving a porous  
58 surface. The start of the nucleation of these droplets is governed by the onset time related to  
59 the solvent evaporation rate, solution concentration and air flow.(22)

60 The factors which regulate the final morphology, like the solvent type (23), concentration(24),  
61 the spinning rate (21) and blend composition (25,26), were already intensively studied.  
62 However, the effect of molecular weight distribution (MWD) is still not well understood.  
63 Regarding the subject of the PTFs, scientific literature focuses mostly at the polymers with  
64 narrow MWD. Conversely, Wu et al. have studied the effect of MWD on the self-assembly of  
65 end-functionalized polystyrenes. They proposed a new way of controlling the morphology of  
66 PTF obtained via breath figures by changing the MWD width. As result the porous membrane  
67 with a higher robustness was obtained.(27)

68 Thus, it should be highlighted that the location and the width of the MWD can affect polymer  
69 solution properties and, as a result, solid thin polymeric films formation. The width of the MWD  
70 can be tailored either within the polymerization process (28,29) or by mixing two polymer  
71 species with very narrow MWD (30). By tailoring the concentration and location of the two  
72 nodes of the distribution of a bimodal polymer, it is possible achieve properties that are  
73 otherwise unavailable.(31) As an example, Heitmiller et al. have reported that the  
74 heterogeneous melt of polyethylene had higher flow index than the homogeneous one.(32) The  
75 investigation performed by the Koningsveld et al. have shown that the bimodal MWD has got  
76 a significant effect on the liquid-liquid binodal curve of polymers in solution. (33) Such a  
77 solution is characterized by phase regions and liquid-liquid phase separation between polymer-  
78 and solvent- rich fractions can occur. Zeman et al. have demonstrated that the critical

79 concentration enabling phase separation in a solution of two polymer species, decreases with  
80 an increase in the molecular weight  $M_w$ .(34) Moreover, even when the polymer – polymer  
81 interactions are athermal, i.e. Flory-Huggins interaction parameter  $\chi$  equals zero, the phase  
82 separation can occur due to the large difference in entropy between long and short chains, which  
83 in fact act as separate entities.(35) This impacts the viscosity of bimodal solutions. Harris et al.  
84 have found that the viscosity of the blend of bimodal polystyrene can be considered as a sum  
85 of components.(36) It has been discussed that blending polystyrenes with different molecular  
86 weight mixed the entanglement types between polymer chains. Furthermore, it was presented  
87 that the concentration of the polymers in the solvent changes how the polymer chains interact.  
88 It was found that two polymer chains, with the same monomer chemical structure, would act as  
89 two different polymers, provided that the concentration is below the overlap concentration ( $C^*$ ).  
90 However, once the overlap concentration occurs, the cooperative motion of the polymer starts  
91 and the behavior of the solution changes. (37,38)

92 Successive research focused on studying how the polymer chains of varying lengths segregate  
93 in PTF. Hariharan et al. investigated the effect of the entropy of spin-coated and annealed  
94 bimodal PTF on polymer chain segregation.(39) It was shown that higher entropy of shorter  
95 chains led to their segregation on the PTF surface, while the lower entropy of the longer chains  
96 promoted their segregation in the bulk. Tanaka et al. in turn studied spin-coated polystyrenes  
97 blends with low and high  $M_w$  with narrow MWD utilizing toluene as a solvent. They reported  
98 that the PTFs consisting of polystyrenes with a low molecular weight demonstrated surface  
99 segregation after thermal treatment.(30) Several other recent studies have illustrated  
100 segregation of lower molecular mass elements towards the surface during annealing.(40–44)

101 On the other hand, it has been shown that segregation of the deuterated polymer can change the  
102 surface roughness after having annealed the coating.(45–48)

103 Despite the extensive studies performed on bimodal polymer solutions and melts, the  
104 segregation during short time scales, for example during spin-coating, when the solid polymer  
105 film is established within few seconds, was not observed until now for pristine polystyrene. In  
106 addition, there is a scarcity of data on spin-coating of polystyrene (PS) in the system with  
107 methyl ethyl ketone (MEK), though MEK is considered to be a marginal solvent for PS.(49,50)  
108 Though, MEK is good choice as a solvent, it is more hydroscopic then typically used solvents  
109 for polystyrene. Thus, it can by a good choice for spin-coating under high humidity conditions.  
110 This article discusses the phase segregation of the low and high molecular weight fractions of  
111 the polystyrene with bimodal MWD dissolved in MEK. The humidity level during the spin  
112 coating process was precisely controlled and spin-coating at humidity ranging up to 75% was  
113 performed. By combining entropic interactions between longer and shorter polymer chains and  
114 interfacial tension between the polymer solution and condensing water from moist air, it was  
115 shown that this conditions leads to a complex morphology consisting of a honeycomb filled  
116 with micropillars.  
117 Additionally, the local mechanical properties of the coatings using atomic force microscopy  
118 were examined. The viscosity parameters of the bimodal blends were tabularized, and the  
119 solubility of the low and high molecular weight polystyrene was discussed.

120

## 121 **2. Experimental**

### 122 **2.1 Materials**

123 All polymers and solvents were purchased from Sigma Aldrich (Merck KGaA). One side  
124 polished ultra-smooth SiO<sub>x</sub> wafers were bought from Technolutions Sp. z o. o.

125

### 126 **2.2 Preparation of the coatings**

127 Analytic standard grade polystyrenes (PS) as obtained from the supplier with PDI = 1.04 and  
 128  $M_w = 20$  kDa, 91 kDa, 150 kDa or 200 kDa, were used.

129 Two kinds of blends were prepared: the blends of 20 kDa and 200 kDa PS mixed in 75/25,  
 130 50/50, 25/75 w/w % proportions; alike the blends of 91 kDa and 200 kDa PS mixed in the same  
 131 proportions. The as prepared PS solutions were being mixed in methyl ethyl ketone (analytic  
 132 grade, MEK), for an hour at 37 °C. After mixing, the solutions were stored overnight. The list  
 133 of polystyrene blends used is summarized in the Table 1. The concentrations of these solution  
 134 ranged from 2.5 mg/ml to 80 mg/ml. Solutions were spin-coated onto a silicon wafers under  
 135 low relative humidity (Rh ~ 0%). DIY Arduino based spin-coater with a chamber with  
 136 controlled humidity was used to spin polystyrene films onto the SiOx wafers. The experimental  
 137 setup is depicted in Supplementary Information (SI) Fig. S1 – S2. A 35  $\mu$ l of the solution was  
 138 pipetted on the 1 cm x 1 cm wafer. The spin-coating was performed in a closed chamber with  
 139 a constant air flow of 10 ml/min of dry air to maintain the desired humidity. The rotational  
 140 speed was 2700 rpm. The spinning time was set to 10 s to allow the solvent to evaporate.

141 For spin-coating in moist atmosphere the relative humidity was changed to 45%, 55% or 75%.  
 142 Again 35  $\mu$ l of the solution (80 mg/ml) was pipetted on the 1 cm x 1 cm wafer and then  
 143 accelerated to 3300 RPM.

144

145 Table 1. List of polymer blends that were used for spin-coating.

Type of Blend	Sample code	Molecular weight $M_w$ [kDa]		PDI
Uniform	20 kDa	20		1.04
	91 kDa	91		1.04
	150 kDa	150		1.04
	200 kDa	200		1.04
Bimodal	Sample code	Molecular weight		PDI
		$[M_w]$ [kDa] <sub>(1)</sub>	$[M_n]$ [kDa] <sub>(2)</sub>	

91 kDa / 200 kDa	75/25*	137	118	1.16
	50/50*	166	146	1.14
	25/75*	186	173	1.08
20 kDa / 200 kDa	75/25**	158	65	2.43
	50/50**	184	110	1.67
	25/75**	194	155	1.25

146 <sup>(1)</sup>Weight average molecular weight  $[M_w] = (f_1M_{w1}^2 + f_2M_{w2}^2) / (f_1M_{w1} + f_2M_{w2})$ , <sup>(2)</sup>Number average molecular  
147 weight  $[M_n] = f_1M_{w1} + f_2M_{w2}$ , where  $f$  - fraction of one of the polymers in %; PDI states for the Polydispersity  
148 index.

149

150 Additionally, two blends: 1) 20 kDa and 200 kDa polystyrene (75/25\*\*) and polymethyl  
151 methacrylate (PMMA, 20 kDa, 1.04 PDI, Sigma Aldrich, polymer standard grade), 7:3 ratio of  
152 bimodal PS to PMMA; 2) 20 kDa and 200 kDa polystyrene (75/25\*\*) and polyvinylpyrrolidone  
153 (PVP, 29 kDa average, Sigma Aldrich), 7:3 ratio of bimodal PS to PVP; were used.

154

### 155 2.3 Gel permeation chromatography (GPC)

156 The number and weight average molecular weights ( $M_n$  and  $M_w$ ) were determined by a modular  
157 system Agilent 1200 series GPC with a refractive index detector (RID) equipped with two  
158 PLgel 5  $\mu$ m MIXED-C columns (300x7.5 mm) in the series, while polydispersity index was  
159 calculated as the ratio of  $M_w/M_n$ . Calibration was performed using a set of 12 narrow-distributed  
160 polystyrene standards with the molecular weight ( $M_p$ ) in the range of 474 g/mol - 1 800 000  
161 g/mol.

162 The measurements were performed at 35 °C, the chloroform GPC grade was used as a solvent  
163 at the flow rate of 0.7 ml/min. All samples (~2 mg/ml) were filtered through PTFE 0.2  $\mu$ m  
164 membrane before the analysis. The data were collected by ChemStation for LC and analyzed  
165 by ChemStation GPC Data Analysis Software.

166

### 167 2.4 Force Spectroscopy FS and Elastic Modulus

168 When a Force Spectroscopy experiment is performed, an AFM probe applies strain on the film  
169 surface. During the process a force/displacement curve is gathered. (51) Force spectroscopy  
170 was performed by means of the atomic force microscope (AFM, Asylum Research MFP3D  
171 Bio). (52) OMLCT-AC200TS-R3 (Olympus) cantilever was used with the nominal spring  
172 constant  $k = 9 \text{ N/m}$  and the tip radius below 10 nm as suggested by the cantilever's producer.  
173 AFM was calibrated using built-in thermal vibrations method. (53) In order to calculate the  
174 elastic modulus (E) from the obtained force/displacement curves a Johnson, Kendall and  
175 Roberts (JKR) model was applied. (54) The indentation depth was  $\sim 8 \text{ nm}$  (Supplementary  
176 Information, 4. *Force Spectroscopy*). As we wanted to neglect the possible influence of stiff  
177 (silica) substrate on registered mechanical data of the polystyrene coating, we decided to  
178 perform FS experiment using the thickest films (films spun from solution of concentration of  
179 80 mg/ml).

180 Maps of large area of the coating  $80 \mu\text{m} \times 80 \mu\text{m}$  with resolution  $40 \times 40$  points were obtained.  
181 These higher resolution maps are supplemented as an attachment (SI). These data were  
182 supported by lower resolution maps with the resolution  $15 \times 15$  points. Each map was used to  
183 obtain the mean elastic modulus value. Altogether, at least 5 maps were made. Ordinary one-  
184 way ANOVA followed by multiple comparisons Fisher's test was used to compare the means  
185 between different groups.

186 Furthermore, histograms representing each higher resolution map were prepared. Skewness of  
187 the elastic modulus distribution was measured. Skewness was divided into two groups: one for  
188 the uniform coatings and one for bimodal coatings. The t test ( $p < 0.05$ ) was used to compare  
189 between the means of these two groups.

190

191 **2.5 Evaluation of thickness of spin-coated films by means of atomic force microscopy**

192 To assess the thickness of the coatings some area was scratched off. The thickness of spin-  
193 coated films was assessed based on the topography images of the scratch, recorded using the  
194 atomic force microscopy technique as shown in SI Fig. S3. Five randomly selected areas of  
195 each sample were tested, and profiles were generated. To avoid any unwanted artefacts,  
196 influence on the profiles, each profile line for analysis was averaged from three contiguous  
197 lines.

198

## 199 **2.6. Imaging of the coatings**

200 The light inverted microscopes (Nikon EPIPHOT 200 and Zeiss Axio Observer) were used for  
201 imaging. The atomic force microscope (AFM, Asylum Research MFP3D Bio) working in the  
202 tapping mode (AC mode) was used to illustrate the phase composition and topography of the  
203 polystyrene films.

204

## 205 **2.7 In-situ measurement of evaporation during spin-coating by means of laser light** 206 **reflectometry with stroboscopic effect**

207 To investigate the thinning of the solution layer while spinning, the in-situ stroboscopic laser  
208 light reflectometry was used. The laser light is reflected from the coating during the spin-  
209 coating process. The occurring interference pattern can be used to estimate the thinning rate of  
210 the solution. (55–57) At the same time, the variability of the amplitude of the degree of  
211 reflection  $\rho$  can be used to characterize the emergence of the interfacial instabilities in the  
212 coating and roughening of the surface when the coating is spun. (58) The experimental setup is  
213 described in SI, Fig. S1 – S2.

214 Depending on the thickness of the layer, constructive or destructive interference can occur.

215 The condition for the constructive interference was calculated from Bragg's law:  $2n\Delta h\cos\theta =$   
216  $m\lambda$ , where  $n$  is the refractive index of the layer,  $\Delta h$  is thickness of the layer,  $\theta$  – incident angle,

217  $m$  is an integer number and  $\lambda$  is light wavelength. For pure MEK  $\Delta h = 235$  nm (assuming the  
218 refractive index  $n_{\text{MEK}} = 1.3788$ ). For the polymer solution it was assumed that the refractive  
219 index was  $n = 1.5$ , thus  $\Delta h = 217$  nm. Laser light wavelength was  $\lambda = 650$  nm.

220

## 221 **2.8 Data analysis and visualization**

222 For data visualization and analysis GraphPad Prism 8 was used. For image analysis procedures  
223 implemented in Gwyddion software (ver 2.50) were used.

224

## 225 **2.9 Fourier Transform IR**

226 To determine the functional groups in the films, infrared spectra were collected using a Fourier  
227 transform infrared spectrophotometer (Nicolet 8700 FTIR, Thermo Scientific). Measurements  
228 were performed using the FTIR ATR over a range of 4000–400  $\text{cm}^{-1}$ .

229

## 230 **2.10 Contact Angle and Surface Free Energy Measurement**

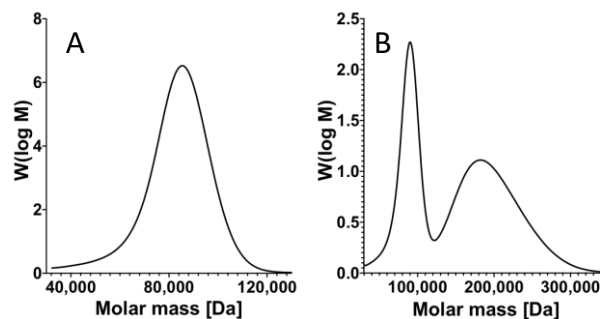
231 The contact angle (CA) was measured using a Data Physics OCA 20 goniometer. The contact  
232 angle was measured with a sessile drop method. For Surface Free Energy measurement (SFE)  
233 two kinds of coatings were chosen: 20 kDa and 200 kDa. For each type of coating 3 droplets  
234 were measured and 3 different coatings were used. Two liquid system was used: deionized  
235 water and diiodomethane (Sigma Aldrich, Analytic grade). The groups were compared with t  
236 test ( $p < 0.05$ ). Owens, Wendt, Rabel and Kaelble (OWKR) method was used for SFE  
237 calculation. (59)

238

## 239 **3. Result and discussion**

240 Spin-coating is often described in the literature as a two-step process. (21,57) First, a polymeric  
241 solution is dropped on a substrate and spread by the inertia of the rotating substrate (so called  
242 flow regime). Subsequently, the solvent evaporates leaving a solid coating.  
243 Notably, manipulating the position of the two nodes in the bimodal MWD can significantly  
244 alter the nature of polymer - polymer interactions in the solution in a controllable manner, thus,  
245 influencing the solution viscosity. In the research the solutions with bimodal MWD were  
246 prepared so that the two nodes in the distribution were clearly separated. The GPC molecular  
247 weight distribution of a single node MWD (uniform) is presented in Fig. 1 A, which illustrates  
248 the MWD of 91 kDa polystyrene with narrow distribution (PDI=1.04), whereas Fig. 1 B  
249 illustrates the MWD with two nodes of a blend of 91 kDa PS with 200 kDa PS, both with narrow  
250 distributions (PDI=1.04). GPC investigation confirmed that the molecular weight and MWD of  
251 each of the component was the same before and after blending.

252



253

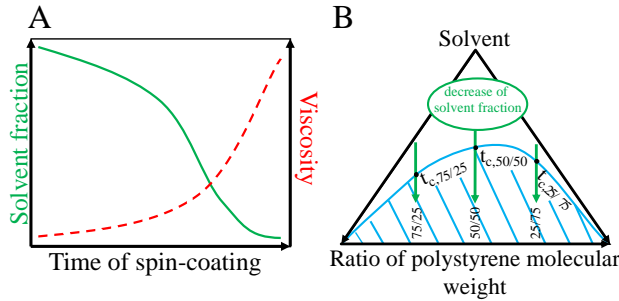
254 Fig 1. Exemplary GPC experiment results of bimodal and uniform MWD polystyrene; A -  
255 narrow uniform MWD,  $M_w = 91$  kDa, PDI 1.04; B – bimodal MWD, blend of  $M_w = 91$  kDa,  
256 PDI = 1.04 and  $M_w = 200$  kDa, PDI = 1.04.

257

258 The evaporation of the solvent through the spin-coating increased the viscosity of the solution.  
259 Successively, the solution concentration fell below the threshold at which the components  
260 cannot coexistence as a one phase (Fig 2A and 2B). The arrows mark the paths of the  
261 evaporation of the 3 tested compositions: 75/25 w/w%, 50/50 and 25/75, respectively. Due to

262 the dissimilarity of the molecular weight of lighter and heavier elements the phase diagram is  
 263 not symmetrical but is shifted towards the lower miscibility of the heavier element.(60)

264



265

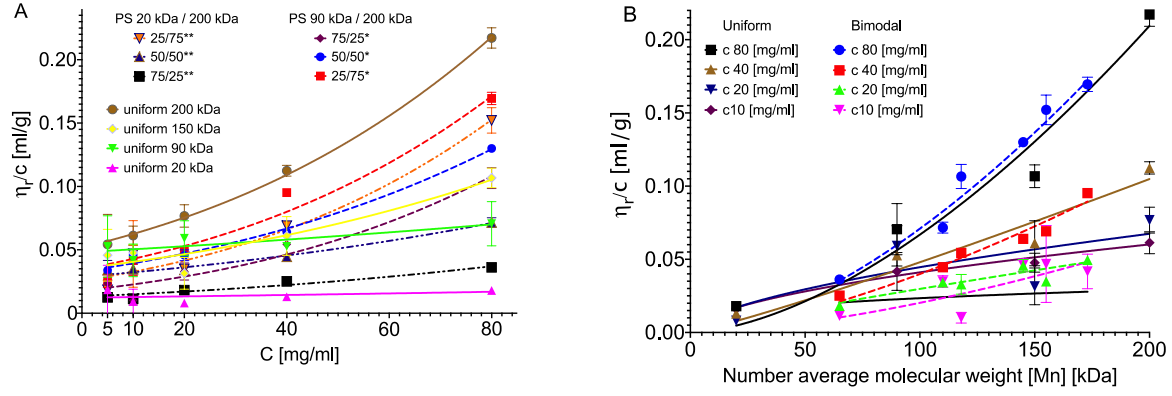
266 Fig. 2 A – Schematic illustration of the change of the solvent fraction and the solution viscosity  
 267 due to the evaporation of the solvent during spin-coating; B – Schematic phase diagram in  
 268 ternary system of polystyrene blend with two molecular weights and solvent. The blue line  
 269 separates the coexistence region from spinodal decomposition region, illustrated by parallel  
 270 lines. The arrows illustrate the path of the system as the solvent evaporates with time,  $t_c$  is the  
 271 time necessary to reach a critical concentration at which two phase region exists. 75/25, 50/50,  
 272 25/75 – different evaporation paths for the aforementioned polystyrene fractions.

273

### 274 3.1 Evaluation of solution viscosities

275 The viscosity measurement (Fig. 3.) can be used to assess not only the final coating thickness  
 276 and the solution evaporation time prediction, but also it can provide information about the  
 277 character of polymer chains interactions. The measurement result is presented as reduced  
 278 viscosity  $\eta_r/c$ , where  $c$  represents concentration in mg/ml. Here  $\eta_r = \frac{\eta - \eta_s}{\eta_s}$ , where  $\eta$  is dynamic  
 279 viscosity of the solution and  $\eta_s$  is the viscosity of the solvent. In Fig. 3A the viscosity is plotted  
 280 as a function of the concentration.

281



282

283 Fig. 3. Reduced viscosity  $\eta_r/c$  of the solutions, A - plotted against the concentration of the  
 284 solution, B in the function of the number average molecular weight,  $[M_n] = f_1M_{w1} + f_2M_{w2}$ ,  
 285 where  $f$  is w/w % ratio of polymers.

286

287 The general dependence of viscosity on concentration can be described in a form of a power  
 288 series:(61)

$$289 \frac{\eta_r}{c} = [\eta](1 + K[\eta]C + \frac{K[\eta]C^2}{2} + \frac{K[\eta]C^3}{6}) \quad (2)$$

290 where  $[\eta]$  is intrinsic viscosity at infinite dilution. The coefficients are summarized in Table S1  
 291 in SI. The difference between bimodal and uniform solution is clearly visible for concentrations  
 292 surpassing the overlap concentration at around 20 mg/ml.(62) It should be noted that the  
 293 viscosity of the bimodal solutions increased faster with the increase of the concentration than  
 294 in case of uniform solutions.

295 Thereafter Fig. 3B presents the viscosity in relation to the number molecular weight  $[M_n]$ . The  
 296 relation between viscosity and molecular weight can be described in a form of the Mark-  
 297 Houwink equation:(61)

$$298 \frac{\eta_r}{c} = \ln K + a \ln[M_n]. \quad (3)$$

299 The  $K$  and  $a$  coefficient values are summarized in SI, Table S2. Again, a variation between the  
 300 behavior of uniform and bimodal solutions was registered, while the uniform solutions were  
 301 visibly more viscous than the bimodal counterpart of similar molecular weight. The positive

302 solvent – polymer interaction causes swelling of polymer chains, which is further reflected in  
 303 the enhanced viscosity of polymeric solution. In such case the interactions between polymer  
 304 chains are more probable. Inversely, the addition of a higher molecular fraction reduces the  
 305 solubility of the polymer. However, for 80 mg/ml the difference disappeared and the viscosity  
 306 – molecular weight curves displayed by similar tendencies.

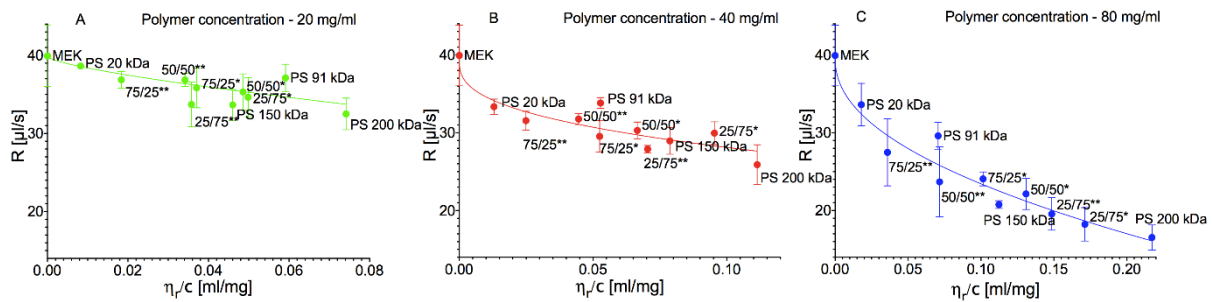
307 In conclusion, the bimodal solution were less viscus than the uniform ones at low concentrations  
 308 ( $c < 20$  mg/ml). However, the viscosity in the case of the bimodal blends rapidly increased with  
 309 the increase of the concentration.

310

### 311 3.2 Evaporation of the solvent during spin-coating

312 Subsequently, the relation between the viscosity (concentrations  $c$ : 20 mg/ml, 40 mg/ml and 80  
 313 mg/ml) of the uniform and bimodal solutions and the evaporation rate of the solutions during  
 314 spin-coating was analyzed (Fig. 4).

315



316

317 Fig. 4. Relation between the evaporation rate of solution and the reduced viscosity of solution  
 318 for polymer concentrations: A - 20 mg/ml, B - 40 mg/ml and C - 80 mg/ml, respectively.

319

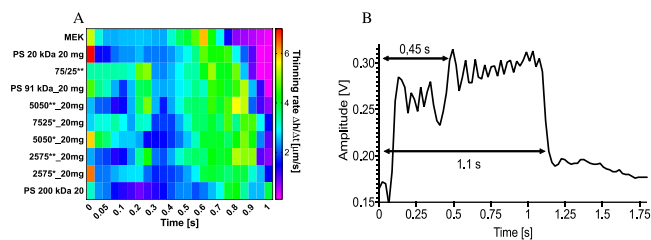
320 Let us now expand the topic of bimodal MWD solution evaporation and compare it with  
 321 evaporation rate of the solution with the homogeneous MWD. The thinning rate is important,  
 322 as it allows to extract the height – time profile and predict the evaporation rate and heat behavior

323 at particular time. Especially, the start of the water droplet condensation coming from humidity  
324 depends on the temperature fluctuations which are related to the evaporation rate.

325 Evaporation of the solutions was measured by laser reflectometry. The intensity of scattered  
326 light increases with solution density, and for higher concentrations clear interference fringes  
327 are hard to obtain. This led to choosing solutions with concentration of exclusively 20 mg/ml  
328 (which is in proximity to the overlap concentration  $C^*$ ) for further investigation.

329 Fig. 5A presents the first second of solution evaporation in a form of a heat map. The heat map  
330 graph (Fig. 5A) presents the thinning rate of the solution ( $\Delta h/\Delta t$ ) in  $\mu\text{m/s}$ , where color of each  
331 pixel corresponds to the thinning rate value. After 1s the thickness of the film decreased enough  
332 for interference to cease. As predicted, the shortest time of this phenomenon was registered for  
333 pure MEK. The measured times increased accordingly to the average molecular weight of the  
334 solution. In case of solutions with added higher molecular weight fraction after turbulent 0.3 s,  
335 a clear region of a slower thinning was found. The region spans between 0.3 s and 0.4 s. Fig.  
336 5B presents the evaporation curve of 50/50 w/w % 91 kDa and 200 kDa solution. Subsequently,  
337 the region of a lowered thinning rate is followed by a region of an increased thinning rate, which  
338 is shifted further in time and prolonged for all solutions with an added fraction of higher  
339 molecular weight. It can be assumed, that this phenomenon can be assigned to liquid-liquid  
340 phase separation on solvent and polymer rich fraction. It is also possible, that addition of the  
341 longer chains facilitates this phase behavior. Then, the behavior of the bimodal solutions would  
342 be a mix of properties of its components. On the other hand, this phenomenon can be associated  
343 with the final morphology formation. If so, the morphology would start to form in a relatively  
344 early stage of the process. Moreover, it can be assumed that the acceleration of evaporation in  
345 the later stage would be responsible for the decrease of surface temperature. This will  
346 subsequently facilitate water condensation.

347



348

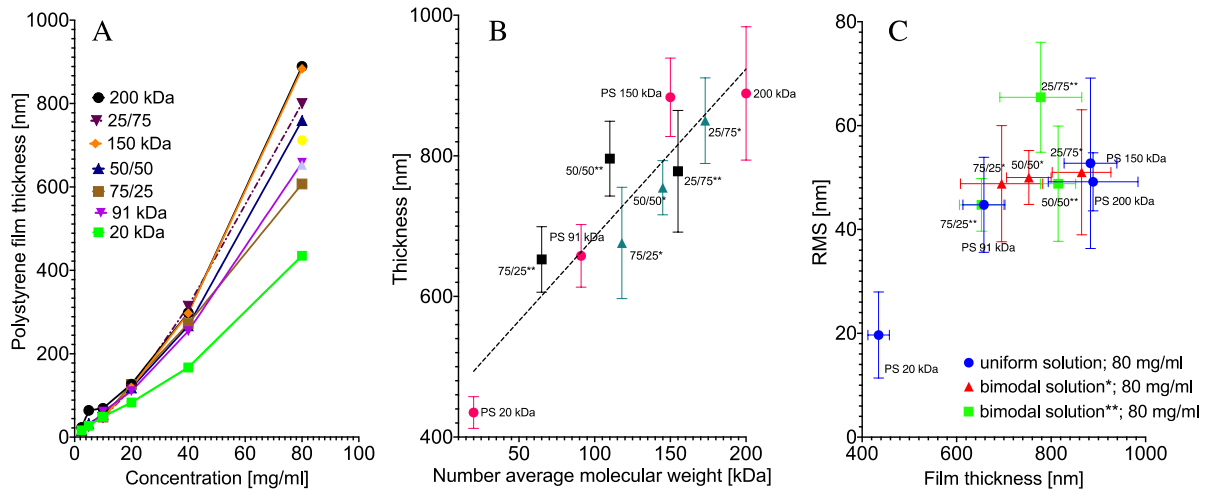
349 Fig. 5. A - Heat map of the thinning rate of the solution during the spin-coating for  
 350 concentration of 20 mg/ml; B – representative evaporation curve of 50/50 w/w % 91 kDa and  
 351 200 kDa solution, concentration 20 mg/ml, vertical axis corresponds to the voltage amplitude  
 352 found on the photodetector and the horizontal axis corresponds to the duration of spin-coating.

353

### 354 3.3 Investigation of the thickness and morphology of the coatings spun at Rh 0%

355 The convection Marangoni flow, solvent evaporation, as well as the phase separation events  
 356 were found to alter the morphology of the coating surface. As a result, occurrence of wrinkles  
 357 or arrays of islands on the surface of the coating was reported. (47,63–65)

358 To determine the effect of bimodal MWD on coating's morphology, the coatings were  
 359 investigated via AFM and optical imaging. Significant differences between blend types  
 360 occurred when the solution concentration was 80 mg/ml (Fig. 6A). As illustrated in Fig. 6B the  
 361 thickness of the coatings in case of 80 mg/ml scaled linearly with the average molecular weight  
 362 of the blends.



364

365 Fig. 6. A - Thickness of the coatings in respect of the composition and the concentration. The  
 366 plot presents data for uniform and 91 kDa / 200 kDa solutions. B – Thickness of the coating for  
 367 the concentration of 80 mg/ml in function of the blend's molecular weight. \* - Blends of 91  
 368 kDa and 200 kDa polystyrene; \*\* - blend of 20 kDa and 200 kDa polystyrene; x/x – w/w% ratio  
 369 of blended homogeneous polystyrenes. The number average molecular weight  $[M_n] = f_1M_{w1} +$   
 370  $f_2M_{w2}$ , where  $f$  w/w. % ratio of polymers. C - RMS roughness of the coatings spun from 80  
 371 mg/ml concentration.

372

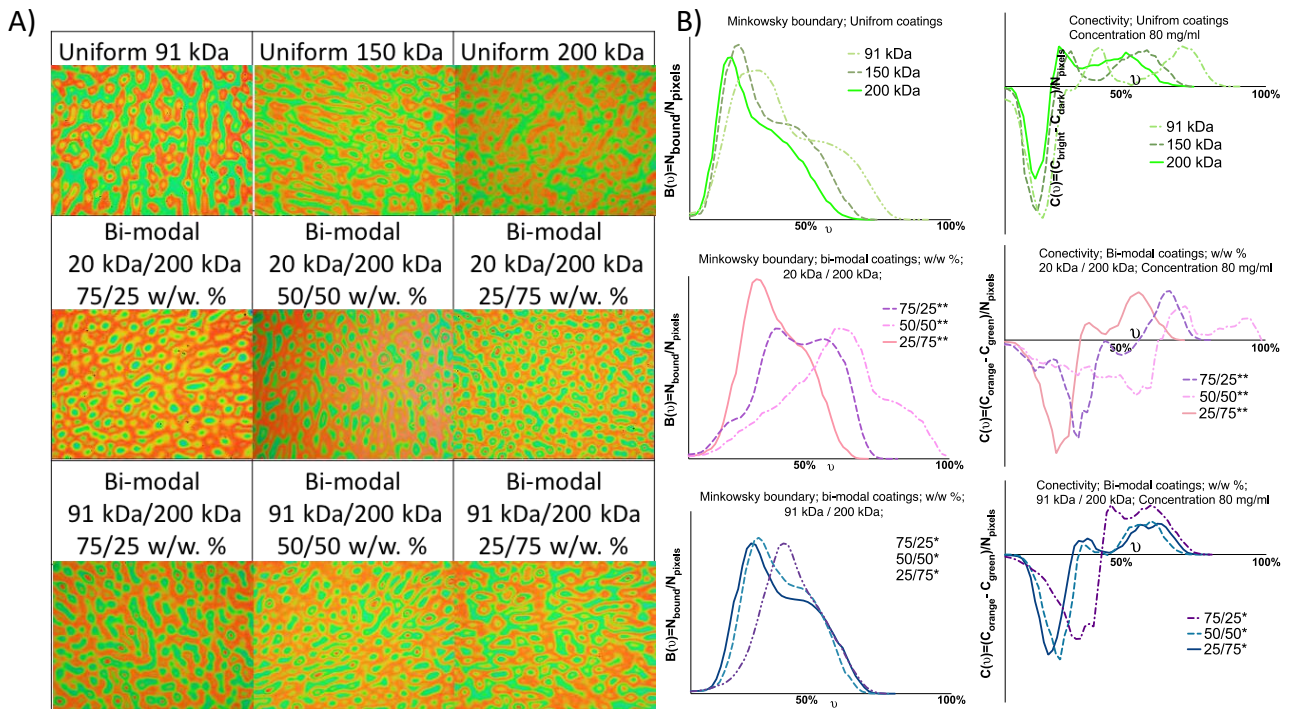
373 In addition it was observed that roughness scales with the film's thickness, the values are not  
 374 significantly different (Fig. 6C). Nonetheless, the similar RMS value can describe an infinite  
 375 number of possible morphologies. In order to represent the morphology of the material  
 376 quantitatively one can apply the Minkowski parameters.(66)

377 The images (Fig. 7A) used for analysis come from the central part of the image, in order to  
 378 exclude the high shear rate effect on the coating's morphology. On the basis of this description,  
 379 it can be concluded that the morphology of the uniform coatings is characterized by separate  
 380 islands (red color in Fig. 7A) surrounded by a bicontinuous green phase. Oppositely, the  
 381 bimodal coatings are characterized by a red bicontinuous phase with separate green islands

382 included. The bicontinuous phase in such case becomes fainter with the increase of the higher  
 383 weight molecular fraction. This occurrence was observed in case of both kinds of bimodal  
 384 blends: 20 kDa / 200 kDa and 91 kDa / 200 kDa.

385 Fig. 7B presents boundary and connectivity. The first of the two parameters, boundary  $B(\nu)$   
 386 characterizes the number of bound pixels at the edge between dark and bright regions in a  
 387 binarized picture at a specific threshold  $\nu$ . Connectivity  $C(\nu)$  can be used to describe the  
 388 bicontinuous or island morphology of the coating in respect to the given binarization threshold  
 389  $\nu$ . The negative value of connectivity corresponds to bicontinuous morphology, while the  
 390 positive value corresponds to island morphology. Together, those two parameters provide a  
 391 relevant description of the surface morphology.

392



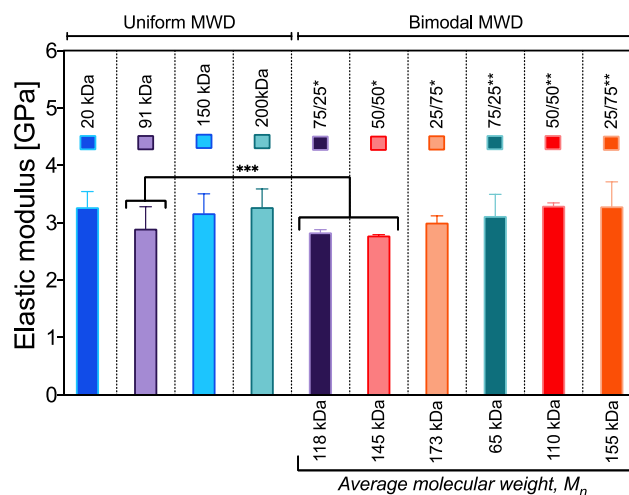
393 Fig. 7. A - Optical images of coatings spun from 80 mg/ml. The B- Minkowski boundary  $B(\nu)$   
 394 and connectivity  $C(\nu)$ , of the coatings spun from 80 mg/ml, where  $\nu$  represents the threshold  
 395 for the image binarization,  $N_{bound}$  is the number of pixels bounded between bright and light  
 396 picture areas at a given threshold,  $N_{pixels}$  is the total number of pixels,  $C_{orange}$  is a total number

397 of orange pixels at a given threshold,  $C_{green}$  is the total number of green pixels at a given  
 398 threshold.

### 399 3.4 Investigation of coatings phase composition by means of AFM Force Spectroscopy

400 AFM Force Spectroscopy method allows to visualize and quantify surface areas differing in  
 401 mechanical properties.(67) The coatings spun from the solutions with the concentration of 80  
 402 mg/ml were studied. By averaging the values from the obtained maps, the resulting elastic  
 403 modulus of the coatings was calculated (Fig. 8).

404



405

406 Fig. 8. Average elastic modulus obtained based on the FS method for coatings made from the  
 407 solution of 80 mg/ml. Uniform – coatings were made from homogeneous solutions; Bimodal –  
 408 coatings made from solutions with bimodal MWD; \* - Blends of 91 kDa and 200 kDa  
 409 polystyrene; \*\* - blend of 20 kDa and 200 kDa polystyrene; x/x – w/w% ratio of blended  
 410 homogeneous polystyrenes.  $[M_n] = f_1M_{w1} + f_2M_{w2}$ , where  $f$  w/w % ratio of polymers. \*\*\* -  
 411 means are significantly different (one-way ANOVA,  $p < 0.05$ ).

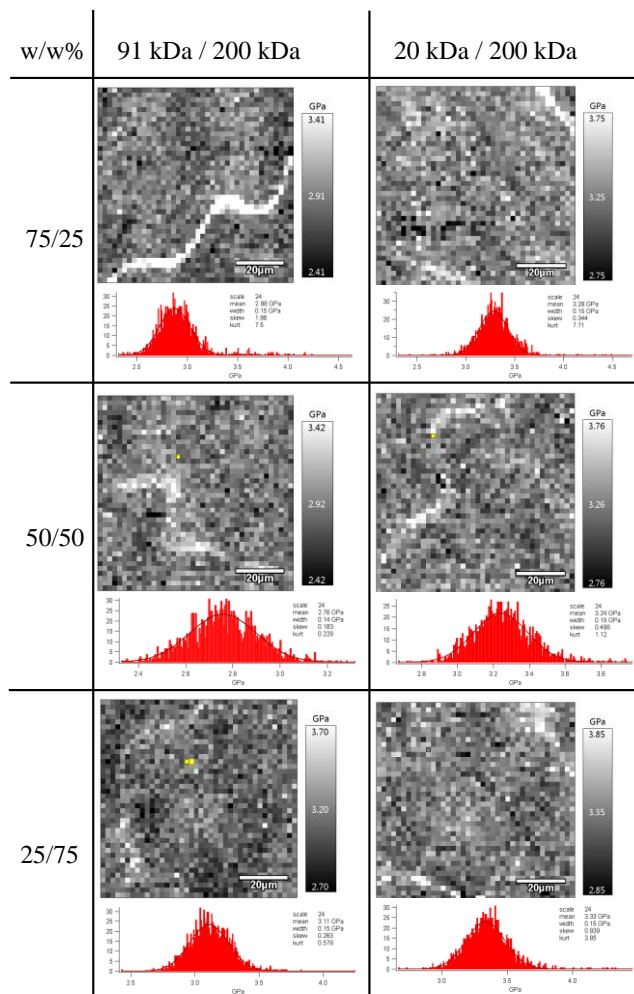
412

413 The obtained results are similar to those found in the literature.(68) The uniform 91 kDa coating  
 414 and the 75/25 and 50/50 blends of 91 kDa and 200 kDa had significantly lower elastic modulus  
 415 than the rest of the tested groups. The dependence between the molecular weight and the elastic

416 modulus of polymer has been repeatedly proven.(69,70) However, we have not found  
417 significant differences between other groups than those mentioned. In our investigation the  
418 uniform 20 kDa coating had similar elastic modulus as the 200 kDa coating. This could have  
419 happened due to the influence of the substrate, as the 20 kDa coating was the thinnest. We have  
420 performed linear regression test (SI, *Force Spectroscopy*, Fig. S4) between the thickness of the  
421 80 mg/ml coatings and the elastic modulus which proved no relationship between the thickness  
422 of the coatings and the elastic modulus, while the 20 kDa coating was an outlier (SI, *Force*  
423 *Spectroscopy*, Table 14).

424 Interestingly, it was possible to record local differences of the coating surface stiffness (Fig. 9).  
425 The maps were gathered for bimodal coatings. White spinodal-like areas are characterized by  
426 higher stiffness. The differences are more clearly visible in case of 90 kDa and 200 kDa blends,  
427 in agreement with Fig. 8.

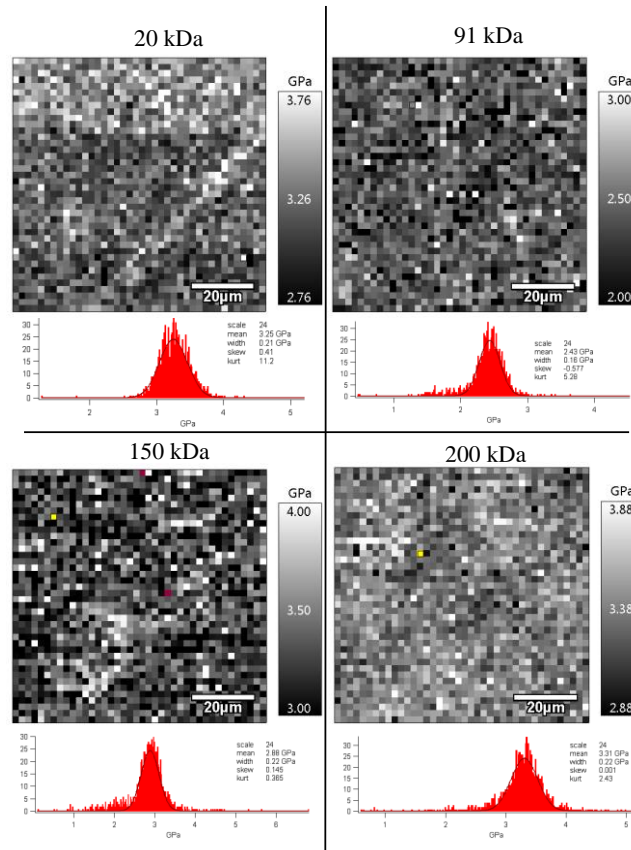
428



429

430 Fig. 9. Force Spectroscopy maps of bimodal MWD coatings. The grey scale shows the stiffness

431 – the white color corresponds to the highest stiffness. The gray scale range is  $\pm 1$  GPa.



432

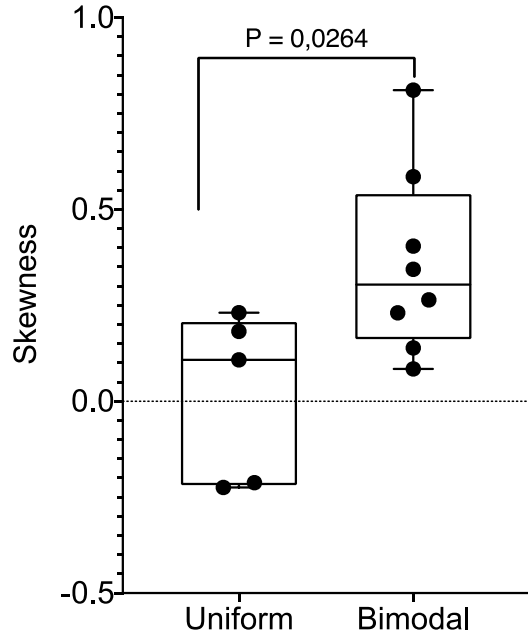
433 Fig. 10. Force Spectroscopy maps of coatings with uniform MWD. The grey scale shows the  
 434 stiffness – the white color corresponds to the highest stiffness. The gray scale range is  $\pm 1$  GPa.

435

436 For comparison, Fig. 10 illustrates the FS maps of the uniform coatings. We have analyzed the  
 437 skewness of the elastic modulus distribution of the maps (SI, *Force Spectroscopy*, Table S15).

438 The skewness in case of uniform coatings was significantly lower ( $p < 0.05$ ) than in case of the  
 439 bimodal coatings (Fig. 11). The distribution of the elastic modulus of the uniform coatings was

440 more homogeneous.



441 Fig 11. Skewness of the elastic modulus data sets. Uniform – grouped means representing  
 442 skewness of histograms of uniform coatings elastic modulus. Bimodal – grouped means  
 443 representing skewness of histograms of all kinds of bimodal blends elastic modulus. The means  
 444 of these two groups are significantly different ( $p < 0.05$ ).  
 445

446

### 447 3.5 Solubility of polystyrenes in respect to the molecular weight distribution

448 The aforementioned, found by FS, phase segregation could be explained by solubility  
 449 investigation. It was shown that viscosity of the polymeric solution can be utilized by  
 450 application of the Mangaraj method to retract several polymer - solvent parameters, i.e. the  
 451 Flory interaction parameter.(71) We utilized the Mangaraj equation (eq.4) in order to  
 452 investigate the miscibility gap between the lower and the higher molecular weight polystyrenes.

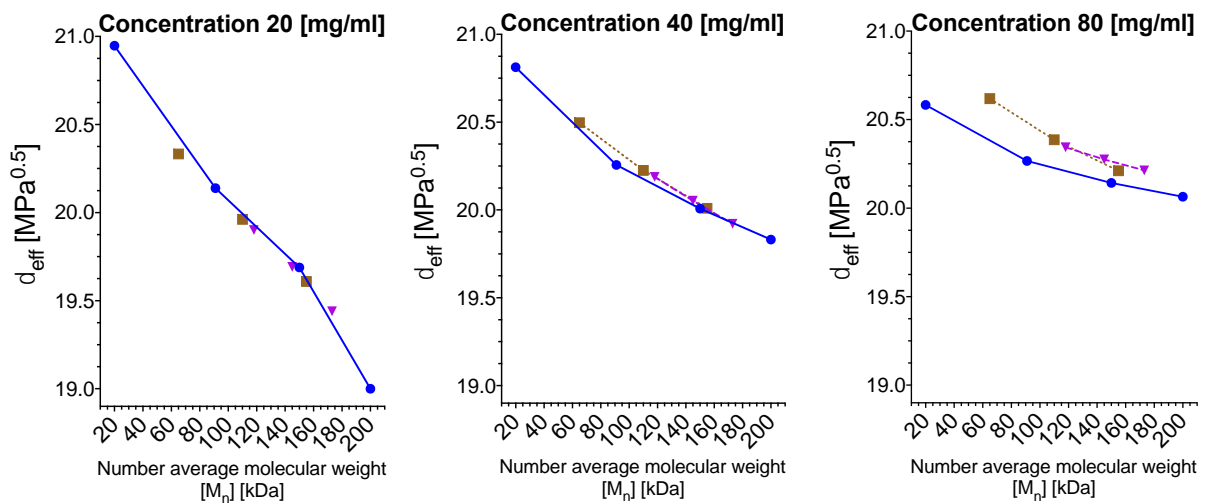
453 (72)

$$454 \ln\left(\frac{\eta}{\eta_{max}}\right) = -(\delta_s - \delta_{eff})^2. \quad (4)$$

455 The effective miscibility parameter  $\delta_{eff}$  was calculated with respect to a solution of 200 kDa  
 456 with concentration of 80 mg/ml which had the highest viscosity among the tested solutions  
 457 ( $\eta_{max}$ ). The parameter of the solvent  $\delta_s$  was set to be  $19 \text{ MPa}^{0.5}$ , which is a typical value for  
 458 MEK.

459 In fact, the miscibility gap between low and high molecular weight polystyrene can be derived  
 460 based on the viscosity of PS blends. Furthermore, the miscibility gap decreases accordingly to  
 461 the low molecular weight fraction. Here,  $\delta_{eff}$  is the effective Hildebrand miscibility parameter  
 462 calculated based on the intrinsic viscosity  $[\eta]$ . In case of the 20 mg/ml concentration, all the  
 463 solutions are present on the same linear trend with the lowest  $\delta_{eff}$  for the highest molecular  
 464 weight. It should be noted that, with concentration increase, the trends for 20 kDa / 200 kDa  
 465 solutions (brown squares), 91 kDa / 200 kDa solutions (purple triangles) and the uniform  
 466 solutions (blue circles) become divergent at low molecular weights, with their trends being  
 467 coincidental at 200 kDa.

468



469

470 Fig. 12. The effective miscibility parameter  $\delta_{eff}$  of the polystyrenes in MEK with bimodal and  
 471 uniform distributions for two kinds of bimodal distributions: 20 kDa / 200 kDa – brown squares  
 472 and 91 kDa / 200 kDa – purple triangles; the blue circles represent data for polystyrenes with  
 473 the uniform distributions.  $[M_n] = f_1M_{w1} + f_2M_{w2}$ , where  $f$  w/w % ratio of polymers.

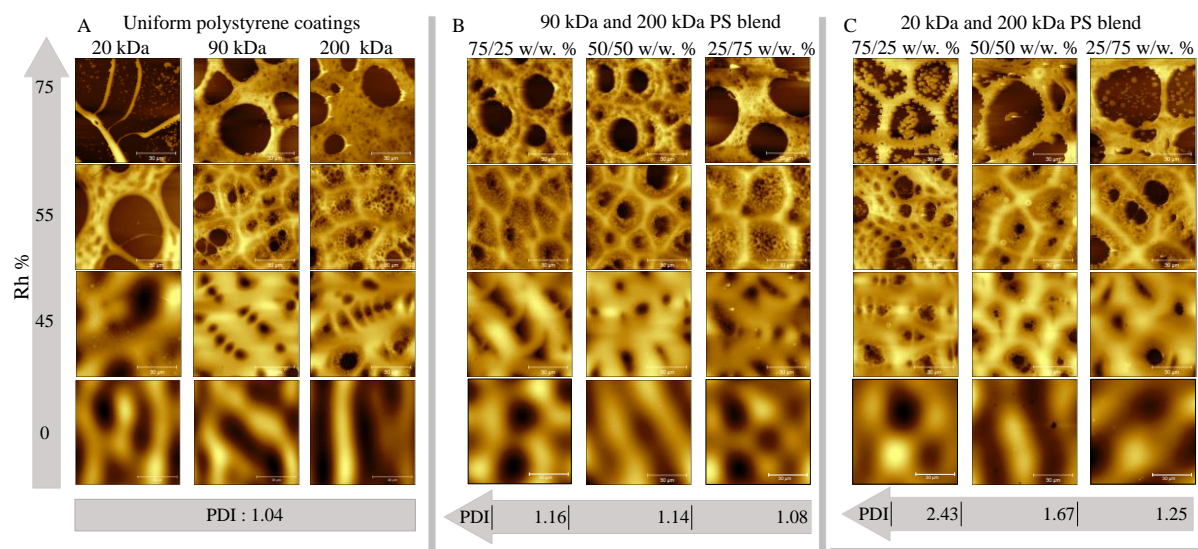
474

### 475 3.5 Self-assembly due to phase segregation and water condensation

476 As a follow-up, we have utilized the humidity in order to take advantage from the phase  
 477 segregation observed above. The viscosity and solubility investigations pointed to

478 concentration of 80 mg/ml in order to obtain the most pronounce effect. It is well established  
 479 method to use the solvent evaporation driven water condensation on the surface of the liquid  
 480 film to cause ruptures in the film. Water droplets immerse in films and consequently at a higher  
 481 water concentration this may lead to gaps in the films. After the droplets evaporated, they left  
 482 cavities inside the film. The condensing water force the film to dewet and retreat from SiO<sub>2</sub>.  
 483 The tested relative humidity Rh values were 45%, 55%, 75%. Fig. 13 A shows images of  
 484 coatings composed of uniform polystyrenes, Fig. 13 B presents images of coatings prepared  
 485 from 91 kDa and 200 kDa blends and Fig. 13 C presents images of coatings prepared from 20  
 486 kDa and 200 kDa blends. Each column is marked below the PDI value of the mixture and each  
 487 row corresponds to one of the Rh values. Optical microscope images show larger area of the  
 488 coatings and are presented in the Supplementary Information, Fig. S6 – S8.

489



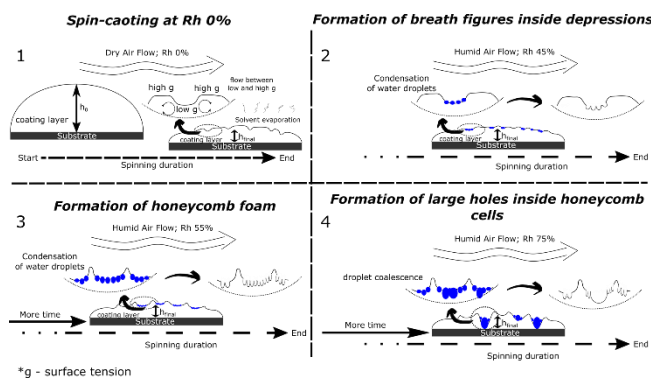
490

491 Fig. 13. Morphology of coatings with bimodal MWD spun under different humidity conditions,  
 492 the solution concentration C was 80 mg/ml. The z-scale was chosen for the best representation  
 493 of the coating's morphology. A – uniform coatings; B – 20 kDa and 200 kDa blends; C – 91  
 494 kDa and 200 kDa blends.

495

496 We have observed that the smaller cavities (breath figures) formed around the larger cavities  
 497 caused by dewetting related polymeric film ruptures. The structure which resembles the  
 498 honeycomb also occurred. Such patterns are often associated with the Bernardo-Marangoni  
 499 convention flowing inside a solidifying polymer film. (73,74) The Bernardo-Marangoni's  
 500 convective flow occurs at a gradient of the surface tension and the evaporation rate. Such  
 501 gradient may occur due to the aforementioned phase morphology of coatings prepared from bi-  
 502 modal blends. For Rh 55% the honeycomb-like morphology is found for all of the coatings,  
 503 except the uniform 20 kDa coating. The proposed process of formation of such complex  
 504 morphology is presented in Fig. 14.

505



506

507 Fig. 14. The chart illustrates the evolution of the morphology of coatings under the influence  
 508 of the flow of humid air. 1 – Spin-coating in dry conditions, convective flow causes surface  
 509 roughening. 2 – Condensation of water droplets if the humidity is Rh 45% results in formation  
 510 of breath figures. 3 – The Marangoni convection and more vapor condensation leads to a  
 511 honeycomb morphology. 4 – Coalescence of water droplets leads to brakeage of the coating  
 512 and formation of large pores inside the honeycomb cells.

513

514 Notably, the uniform coatings have lost their honeycomb morphologies, when humidity Rh  
 515 75% was used. The bimodal coating of 91 kDa and 200 kDa, 25/75 w/w% also did not retain  
 516 the honeycomb morphology. It should be noted that this kind of coating was the most similar

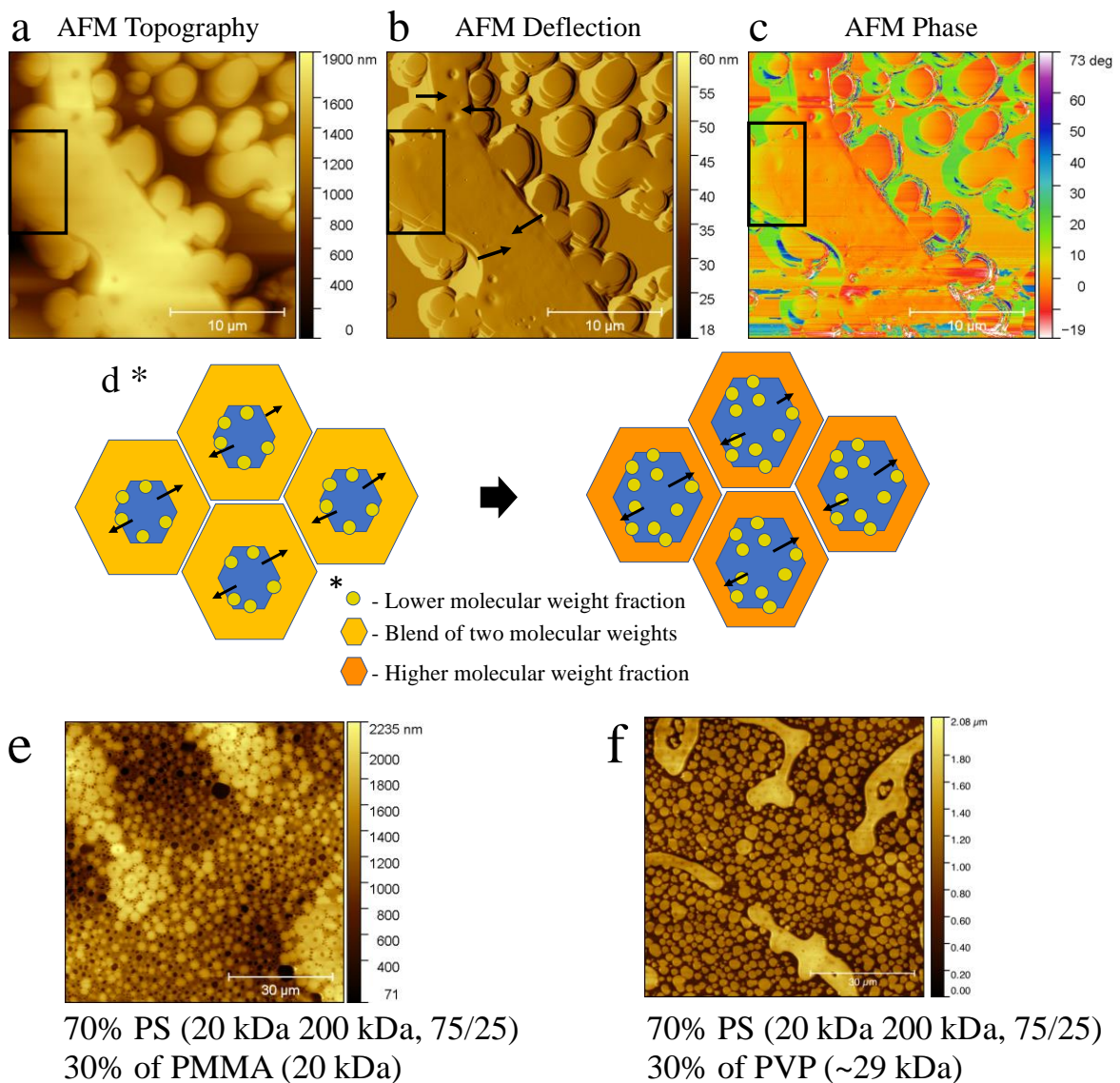
517 to the uniform coatings during optical imaging and force spectroscopy. Radially averaged  
518 Power Spectra Density analysis (SI, Fig. S9) of averaged 4 images depicts the differences  
519 between the 75/25, 50/50 and 25/75 w/w% 20 kDa and 200 kDa coatings.

520 Interestingly, the coatings prepared from 20 kDa and 200 kDa bimodal blends at Rh 75% had  
521 polymeric pillars inside the large holes. It was found that a certain phase in the polymer film  
522 was segregated into structures resembling pillars. An onset of such structures can be observed  
523 also in case of coatings prepared in Rh 55%, but the length of the process in this case was too  
524 short for full pillar formation. The fraction of the pillars decreased with the increase of 200 kDa  
525 contribution. Thus, it can be concluded that the pillars are made of the lower molecular weight  
526 fraction. Additionally, we have tested the formation of the micropillars when a short spin-  
527 coating time was used (0.5s and 1s). These images are presented in Fig. S15 in SI. The phase  
528 segregation was already seen, though, the pillars were not well formed. These results would  
529 confirm the reflectometry experiment, which indicated, that the phase separation could happen  
530 early on during the spin-coating. Nonetheless, the longer spin-coating time is necessary for  
531 enough water condensation to induce the pillar formation.

532 Apparently, as the polymer film receded from the substrate surface, segregation into fractions  
533 of varying weight occurred which led to formation of these structures. It was assumed that the  
534 pillars are made of the lighter and less viscous fraction. Seemingly, the heavier polymer  
535 fraction, more viscous and more entangled reinforced the honeycomb cells borders.

536 Phase segregation was captured by the AFM image (Fig. 15 a - c). The black rectangle indicates  
537 the area that differed in terms of deflection signal and phase contrast. It was observed that  
538 between this area and the rest of the film was separated by cracks. The water condensation of  
539 forced the liquid PS film to dewet from the SiO<sub>2</sub>. The direction of dewetting is marked by black  
540 arrows. The low molecular weight segregated and separated from the main of the film part of

541 the film and formed pillars. The proposed mechanism of pillar formation is depicted in Fig 15  
 542 d.



543  
 544 Fig. 15. AFM picture of 20 kDa and 200 kDa 75/25 w/w% blend spun at Rh 75%, the same  
 545 region is shown in form of a - topography, b - AFM deflection and c - AFM phase images.  
 546 Black arrows mark the direction of dewetting; d – schematic illustration depicting proposed  
 547 pillar formation mechanism; Convection inside the liquid film led to cells formation,  
 548 condensation of water led to film rupture (Blue). Subsequently, recess of the film occurred. At  
 549 the interface between the rupture area and the receding film segregation of lower molecular  
 550 fraction occurred (Yellow). Later, the borders of the cells from remaining high molecular

551 weight fraction (Orange); e, f – Blends of 70% of PS with bimodal MWD and PMMA or PVP,  
552 respectively.

553 As was mentioned, the polystyrenes used were unmodified standard grade polymers. The  
554 unchanged chemical composition of the coatings was confirmed by FTIR spectroscopy (SI Fig.  
555 S10 – S12). The recognized functional groups were CH<sub>3</sub>, CH<sub>2</sub>, and phenyl groups. All of these  
556 groups are hydrophobic and were the driving force behind the dewetting process under high  
557 humidity conditions. These argument was further reinforced by the Free Surface Energy (SEF)  
558 measurement (SI Fig. S13 – S14). The SEF of 20 kDa coating was slightly higher than the 200  
559 kDa coating and in consequence lead to higher affinity to the hydrophilic SiO<sub>2</sub> substrate of the  
560 former one.

561 Finally, in order to test if the described process can be extended to the other polymer systems,  
562 the blends of bi-modal polystyrene and commercially available PMMA or PVP were prepared  
563 and spin-coated. In both cases (Fig. 15e and f), segregation of the polystyrene fractions allowed  
564 to obtain bimodal morphology of larger and smaller islands.

565

## 566 **Conclusions**

567 To summarize, polystyrene solutions either with uniform molecular weight distribution or with  
568 bimodal molecular weight distribution were used. The bimodal blends consisted either of 20  
569 kDa and 200 kDa or of 91 kDa and 200 kDa molecules and 75/25, 50/50 and 25/75 w/w %  
570 ratios of these molecules were applied. The blends were dissolved in methyl ethyl ketone and  
571 used for spin-coating.

- 572 • The viscosity of the solutions with bimodal blend distribution was lower than of the  
573 uniform solutions (< 20 mg/ml) but increased rapidly with increase of the concentration.  
574 The viscosity parameters were tabulated.

- 575 • The viscosity data were applied to determine the solubility parameters of bimodal and  
576 uniform polystyrene. It was concluded that if the polydispersity of the mixture is high  
577 enough, both components of the polystyrene blend can act as separate species and  
578 segregate during spin-coating.
- 579 • The evaporation pattern during spin-coating and evaporation rate was characterized for  
580 each of the polystyrene blends. It was found that bimodal solutions have period of  
581 lowered evaporation rate at around 0.4 s of spin-coating.
- 582 • The morphology of the bimodal coatings characterized by Minkowski measures and it  
583 was concluded that they differ from the morphology of uniform coatings. These result  
584 suggested that the convection flow during spinning in the bimodal solutions is different  
585 as compare to the uniform solutions.
- 586 • Force Spectroscopy reveled spinodal like features in case of the bimodal coatings. These  
587 features were visible in both kinds of bimodal blends, when the ratio was 75 to 25.
- 588 • It was concluded that the segregation into low and high molecular fractions occurred.
- 589 • As the polystyrene is slightly hydrophobic, while the solvent (methyl ethyl ketone) is  
590 slightly hydroscopic, it was concluded that the phase separation can be enhanced by  
591 spin-coating in high humidity. Coating in relative humidity of 45%, 55% and 75% was  
592 tested. It was found, that for 20 kDa and 200 kda blend, at the highest humidity the  
593 polystyrene segregated into pillars formed from the lower molecular weight fraction.  
594 The higher molecular weight fraction formed the honeycomb cells. It was concluded  
595 that these happed due to the difference in viscosity and free surface energy between the  
596 two fractions.
- 597 It was shown that these phenomenon can be extended into other polymer systems in order to  
598 obtain complex and controlled morphology. It is likely possible to apply the described process  
599 to other coatings methods, for example dip coating or inkjet printing.

600

601 **Supporting Information (SI)**

602 Experimental setup depicting the custom build spin-coater with a humidity-controlled chamber  
603 and an in-situ reflectometer utilizing stroboscopic effect. Illustration of thickness measurement.  
604 Viscosity related coefficients. Optical microscope images. FTIR results. Free Surface Energy  
605 results.

606

607 **Author information**

608 Corresponding authors:

609 Maciej Łojkowski, ORCID: 0000-0002-0612-7964, email: [00183042@pw.edu.pl](mailto:00183042@pw.edu.pl)

610 Wojciech Swieszkowski, ORCID: 0000-0003-4216-9974, email:

611 [wojciech.swieszkowski@pw.edu.pl](mailto:wojciech.swieszkowski@pw.edu.pl).

612

613 The authors declare no competing financial interest.

614

615 **Acknowledgments**

616 This manuscript is a part of Maciej Łojkowski PhD thesis. This work was supported by  
617 the National Centre for Research and Developments  
618 [STRATEGMED3/306888/3/NCBR/2017]. We are grateful miss Mgr. Donata Kuczyńska-  
619 Zemła for help with optical microscopy.

620

621 **Authors contributions:**

622 Conceptualization, M.Ł.; methodology, M.Ł., A.Ch., E.Ch.; investigation, M.Ł., A.Ch., E. Ch.,  
623 imaging, M.Ł., A.Ch.; data analysis, M.Ł.; visualization, M.Ł.; writing, M.Ł.; supervision, W.

624 Ś.; revision of the manuscript, M.Ł., A.Ch., E. Ch., W. Ś; funding acquisition W. Ś. All authors  
625 have read and agreed to the published version of the manuscript.

626

## 627 **Abbreviations**

628 AFM – atomic force microscopy; bimodal – polymer with two nodes in molecular weight  
629 distribution; coating – final polymer coating; CA – Contact Angle; E – elastic modulus; film –  
630 liquid film of solution spread on the substrate; FS – force spectroscopy; FTIR – Fourier  
631 Transform IR; GPC – Gel permeation chromatography; initial solution – solution at the start  
632 of spin-coating; MEK – Methyl Ethyl Ketone; Mw – molecular weight;  $[M_w]$  – Weight average  
633 molecular weight;  $[M_n]$  – Number average molecular weight; MWD – molecular weight  
634 distribution; PDI – Polydispersity index; PTF – Polymer thin film; PS – Polystyrene; Rh% -  
635 relative humidity in %; RMS – root mean square roughness; Uniform – polymer with one node  
636 in molecular weight distribution.

637

## 638 **References**

- 639 1. Kumar M, Bhardwaj R. Wetting characteristics of *Colocasia esculenta* (Taro) leaf and a  
640 bioinspired surface thereof. *Sci Rep.* 2020;10(1):1–15.
- 641 2. He R, Xiao J, Zhang M, Zhang Z, Zhang W, Cao Y, et al. Artificial honeycomb-  
642 inspired TiO<sub>2</sub> nanorod arrays with tunable nano/micro interfaces for improving  
643 poly(dimethylsiloxane) surface hydrophobicity. *J Mater Sci.* 2016;51(6):2935–41.
- 644 3. Jahed Z, Shahsavan H, Verma MS, Rogowski JL, Seo BB, Zhao B, et al. Bacterial  
645 Networks on Hydrophobic Micropillars. *ACS Nano.* 2017;11(1):675–83.
- 646 4. Liu X, Liu R, Cao B, Ye K, Li S, Gu Y, et al. Subcellular cell geometry on micropillars  
647 regulates stem cell differentiation. *Biomaterials* [Internet]. 2016;111:27–39. Available  
648 from: <http://dx.doi.org/10.1016/j.biomaterials.2016.09.023>

- 649 5. Walheim S, Böltau M, Mlynek J, Krausch G, Steiner U. Structure Formation via  
650 Polymer Demixing in Spin-Cast Films. *Macromolecules* [Internet]. 1997 Aug  
651 1;30(17):4995–5003. Available from: <https://doi.org/10.1021/ma9619288>
- 652 6. Daly R, Sader JE, Boland JJ. The dominant role of the solvent–water interface in water  
653 droplet templating of polymers. *Soft Matter* [Internet]. 2013;9(33):7960. Available  
654 from: <http://xlink.rsc.org/?DOI=c3sm51452h>
- 655 7. Khikhlovskiy V, Wang R, van Breemen AJJM, Gelinck GH, Janssen RAJ, Kemerink  
656 M. Nanoscale Organic Ferroelectric Resistive Switches. *J Phys Chem C* [Internet].  
657 2014 Feb 13;118(6):3305–12. Available from:  
658 <https://pubs.acs.org/doi/10.1021/jp409757m>
- 659 8. D’Andrade BW, Forrest SR. White Organic Light-Emitting Devices for Solid-State  
660 Lighting. *Adv Mater* [Internet]. 2004 Sep 16;16(18):1585–95. Available from:  
661 <http://doi.wiley.com/10.1002/adma.200400684>
- 662 9. Yabu H. Fabrication of honeycomb films by the breath figure technique and their  
663 applications. *Sci Technol Adv Mater* [Internet]. 2018;19(1):802–22. Available from:  
664 <https://doi.org/10.1080/14686996.2018.1528478>
- 665 10. Wu D, Xu F, Sun B, Fu R, He H, Matyjaszewski K. Design and Preparation of Porous  
666 Polymers. *Chem Rev* [Internet]. 2012 Jul 11;112(7):3959–4015. Available from:  
667 <https://pubs.acs.org/doi/10.1021/cr200440z>
- 668 11. Karagkiozaki V, Vavoulidis E, Karagiannidis PG, Gioti M, Fatouros DG, Vizirianakis  
669 IS, et al. Development of a nanoporous and multilayer drug-delivery platform for  
670 medical implants. *Int J Nanomedicine*. 2012;7(October):5327–38.
- 671 12. Calejo MT, Ilmarinen T, Skottman H, Kellomäki M. Breath figures in tissue  
672 engineering and drug delivery: State-of-the-art and future perspectives. Vol. 66, *Acta*  
673 *Biomaterialia*. 2018.

- 674 13. Vendra VK, Wu L, Krishnan S. Polymer Thin Films for Biomedical Applications. In:  
675 Nanotechnologies for the Life Sciences [Internet]. Weinheim, Germany: Wiley-VCH  
676 Verlag GmbH & Co. KGaA; 2011. Available from:  
677 <http://doi.wiley.com/10.1002/9783527610419.ntls0179>
- 678 14. Griesser HJ. Thin Film Coatings for Biomaterials and Biomedical Applications, 1st  
679 Edition. 2016. 310 p.
- 680 15. Łojkowski M, Walheim S, Jokubauskas P, Schimmel T, Świążkowski W. Tuning the  
681 wettability of a thin polymer film by gradually changing the geometry of nanoscale  
682 pore edges. *Langmuir* [Internet]. 2019;35(17):5987–96. Available from:  
683 <https://doi.org/10.1021/acs.langmuir.9b00467>
- 684 16. Plawsky JL, Kim JK, Schubert EF. Engineered nanoporous and nanostructured films.  
685 *Mater Today* [Internet]. 2009;12(6):36–45. Available from:  
686 [http://dx.doi.org/10.1016/S1369-7021\(09\)70179-8](http://dx.doi.org/10.1016/S1369-7021(09)70179-8)
- 687 17. Bormashenko E. Breath-figure self-assembly, a versatile method of manufacturing  
688 membranes and porous structures: Physical, chemical and technological aspects.  
689 *Membranes* (Basel). 2017;7(3).
- 690 18. van Franeker JJ, Westhoff D, Turbiez M, Wienk MM, Schmidt V, Janssen RAJ.  
691 Controlling the Dominant Length Scale of Liquid-Liquid Phase Separation in Spin-  
692 coated Organic Semiconductor Films. *Adv Funct Mater* [Internet]. 2015  
693 Feb;25(6):855–63. Available from: <http://doi.wiley.com/10.1002/adfm.201403392>
- 694 19. Schaefer C, Michels JJ, van der Schoot P. Structuring of Thin-Film Polymer Mixtures  
695 upon Solvent Evaporation. *Macromolecules* [Internet]. 2016 Sep 27;49(18):6858–70.  
696 Available from: <https://pubs.acs.org/doi/10.1021/acs.macromol.6b00537>
- 697 20. Ebbens S, Hodgkinson R, Parnell AJ, Dunbar A, Martin SJ, Topham PD, et al. In Situ  
698 Imaging and Height Reconstruction of Phase Separation Processes in Polymer Blends

- 699 during Spin Coating. ACS Nano [Internet]. 2011 Jun 28;5(6):5124–31. Available from:  
700 <https://pubs.acs.org/doi/10.1021/nn201210e>
- 701 21. Danglad-Flores J, Eickelmann S, Riegler H. Deposition of polymer films by spin  
702 casting: A quantitative analysis. Chem Eng Sci [Internet]. 2018 Apr;179:257–64.  
703 Available from: <https://linkinghub.elsevier.com/retrieve/pii/S0009250918300125>
- 704 22. Daly R, Sader JE, Boland JJ. Taming Self-Organization Dynamics to Dramatically  
705 Control Porous Architectures. ACS Nano [Internet]. 2016 Mar 22;10(3):3087–92.  
706 Available from: <https://pubs.acs.org/doi/10.1021/acsnano.5b06082>
- 707 23. Müller-Buschbaum P, Gutmann JS, Wolkenhauer M, Kraus J, Stamm M, Smilgies D,  
708 et al. Solvent-Induced Surface Morphology of Thin Polymer Films. Macromolecules  
709 [Internet]. 2001 Feb;34(5):1369–75. Available from:  
710 <https://pubs.acs.org/doi/10.1021/ma0009193>
- 711 24. Bornside DE. Spin Coating of a PMMA/Chlorobenzene Solution. J Electrochem Soc  
712 [Internet]. 1991;138(1):317. Available from:  
713 <https://iopscience.iop.org/article/10.1149/1.2085563>
- 714 25. Wodo O, Ganapathysubramanian B. Modeling morphology evolution during solvent-  
715 based fabrication of organic solar cells. Comput Mater Sci [Internet]. 2012;55:113–26.  
716 Available from: <http://dx.doi.org/10.1016/j.commatsci.2011.12.012>
- 717 26. Huang C, Förste A, Walheim S, Schimmel T. Polymer blend lithography for metal  
718 films: Large-area patterning with over 1 billion holes/inch<sup>2</sup>. Beilstein J Nanotechnol.  
719 2015;6(1):1205–11.
- 720 27. Wu BH, Zhong QZ, Xu ZK, Wan LS. Effects of molecular weight distribution on the  
721 self-assembly of end-functionalized polystyrenes. Polym Chem. 2017;8(29):4290–8.
- 722 28. Jiang H, Zhang L, Qin J, Zhang W, Cheng Z, Zhu X. Producing bimodal molecular  
723 weight distribution polymers through facile one-pot/one-step RAFT polymerization. J

- 724 Polym Sci Part A Polym Chem. 2012;50(19):4103–9.
- 725 29. Whitfield R, Parkatzidis K, Truong NP, Junkers T, Anastasaki A. Tailoring Polymer  
726 Dispersity by RAFT Polymerization: A Versatile Approach. Chem [Internet]. 2020  
727 Jun;6(6):1340–52. Available from:  
728 <https://linkinghub.elsevier.com/retrieve/pii/S2451929420301923>
- 729 30. Tanaka K, Takahara A, Kajiyama T. Effect of Polydispersity on Surface Molecular  
730 Motion of Polystyrene Films. Macromolecules [Internet]. 1997 Oct;30(21):6626–32.  
731 Available from: <https://pubs.acs.org/doi/10.1021/ma970057e>
- 732 31. Zabusky HH, Heitmiller RF. Properties of high density polyethylenes with bimodal  
733 molecular weight distribution. Polym Eng Sci. 1964;4(1):17–21.
- 734 32. Heitmiller RF, Naar RZ, Zabusky HH. Effect of homogeneity on viscosity in capillary  
735 extrusion of polyethylene. J Appl Polym Sci [Internet]. 1964 Mar;8(2):873–80.  
736 Available from: <http://doi.wiley.com/10.1002/app.1964.070080226>
- 737 33. Koningsveld R, Chermin HAG, Gordon M. Liquid–liquid phase separation in  
738 multicomponent polymer solutions - VIII. Stability limits and consolute states in quasi-  
739 ternary mixtures. Proc R Soc London A Math Phys Sci [Internet]. 1970 Oct  
740 27;319(1538):331–49. Available from:  
741 <https://royalsocietypublishing.org/doi/10.1098/rspa.1970.0182>
- 742 34. Zeman L, Patterson D. Effect of the Solvent on Polymer Incompatibility in Solution.  
743 Macromolecules [Internet]. 1972 Jul;5(4):513–6. Available from:  
744 <https://pubs.acs.org/doi/abs/10.1021/ma60028a030>
- 745 35. Shultz AR, Flory PJ. Phase Equilibria in Polymer—Solvent Systems 1,2. J Am Chem  
746 Soc [Internet]. 1952 Oct 1;74(19):4760–7. Available from:  
747 <https://doi.org/10.1021/ja01139a010>
- 748 36. Harris EK. Effect of blending on the rheological properties of polystyrene. J Appl

- 749 Polym Sci [Internet]. 1973 Jun;17(6):1679–92. Available from:  
750 <http://doi.wiley.com/10.1002/app.1973.070170604>
- 751 37. Klein J. The Onset of Entangled Behavior in Semidilute and Concentrated Polymer  
752 Solutions. *Macromolecules* [Internet]. 1978 Sep;11(5):852–8. Available from:  
753 <https://pubs.acs.org/doi/abs/10.1021/ma60065a002>
- 754 38. Hong KM, Noolandi J. Theory of inhomogeneous multicomponent polymer systems.  
755 *Macromolecules* [Internet]. 1981 May;14(3):727–36. Available from:  
756 <https://pubs.acs.org/doi/abs/10.1021/ma50004a051>
- 757 39. Hariharan A, Kumar SK, Russell TP. A lattice model for the surface segregation of  
758 polymer chains due to molecular weight effects. *Macromolecules* [Internet]. 1990  
759 Jul;23(15):3584–92. Available from:  
760 <https://pubs.acs.org/doi/abs/10.1021/ma00217a009>
- 761 40. Mahmoudi P, Matsen MW. Entropic segregation of short polymers to the surface of a  
762 polydisperse melt. *Eur Phys J E* [Internet]. 2017 Oct 6;40(10):85. Available from:  
763 <http://link.springer.com/10.1140/epje/i2017-11575-7>
- 764 41. Hill JA, Endres KJ, Mahmoudi P, Matsen MW, Wesdemiotis C, Foster MD. Detection  
765 of Surface Enrichment Driven by Molecular Weight Disparity in Virtually  
766 Monodisperse Polymers. *ACS Macro Lett* [Internet]. 2018 Apr 17;7(4):487–92.  
767 Available from: <https://pubs.acs.org/doi/10.1021/acsmacrolett.7b00993>
- 768 42. Stein GE, Laws TS, Verduzco R. Tailoring the Attraction of Polymers toward Surfaces.  
769 *Macromolecules* [Internet]. 2019 Jul 9;52(13):4787–802. Available from:  
770 <https://pubs.acs.org/doi/10.1021/acs.macromol.9b00492>
- 771 43. Carlier V, Sclavons M, Jonas AM, Jérôme R, Legras R. Probing Thermoplastic  
772 Matrix–Carbon Fiber Interphases. 1. Preferential Segregation of Low Molar Mass  
773 Chains to the Interface. *Macromolecules* [Internet]. 2001 May;34(11):3725–9.

- 774 Available from: <https://pubs.acs.org/doi/10.1021/ma000404b>
- 775 44. Suwa J, Kakiage M, Yamanobe T, Komoto T, Uehara H. Molecular Weight  
776 Segregation on Surfaces of Polyethylene Blended Films as Estimated from  
777 Nanoscratch Tests Using Scanning Probe Microscopy. *Langmuir* [Internet]. 2007  
778 May;23(11):5882–5. Available from: <https://pubs.acs.org/doi/10.1021/la070150o>
- 779 45. Karim A, Slawecki TM, Kumar SK, Douglas JF, Satija SK, Han CC, et al. Phase-  
780 Separation-Induced Surface Patterns in Thin Polymer Blend Films. *Macromolecules*  
781 [Internet]. 1998 Feb;31(3):857–62. Available from:  
782 <https://pubs.acs.org/doi/10.1021/ma970687g>
- 783 46. Hoppe H, Heuberger M, Klein J. Self-Similarity and Pattern Selection in the  
784 Roughening of Binary Liquid Films. *Phys Rev Lett* [Internet]. 2001 May  
785 21;86(21):4863–6. Available from:  
786 <https://link.aps.org/doi/10.1103/PhysRevLett.86.4863>
- 787 47. Heier J, Kramer EJ, Revesz P, Battistig G, Bates FS. Spinodal Decomposition in a  
788 Subsurface Layer of a Polymer Blend Film. *Macromolecules* [Internet]. 1999  
789 Jun;32(11):3758–65. Available from: <https://pubs.acs.org/doi/10.1021/ma981709h>
- 790 48. Jandt KD, Heier J, Bates FS, Kramer EJ. Transient surface roughening of thin films of  
791 phase separating polymer mixtures. *Langmuir*. 1996;12(15):3716–20.
- 792 49. Flory PJ, Höcker H. Thermodynamics of polystyrene solutions. Part 1.—Polystyrene  
793 and methyl ethyl ketone. *Trans Faraday Soc* [Internet]. 1971;67:2258–69. Available  
794 from: <http://xlink.rsc.org/?DOI=TF9716702258>
- 795 50. Imre A, Van Hook WA. Liquid-liquid demixing from solutions of polystyrene. 1. A  
796 review. 2. Improved correlation with solvent properties. Vol. 25, *Journal of Physical*  
797 *and Chemical Reference Data*. 1996. p. 637–61.
- 798 51. Zgłobicka I, Chlanda A, Woźniak M, Łojkowski M, Szoszkiewicz R, Mazurkiewicz-

- 799 Pawlicka M, et al. Microstructure and nanomechanical properties of single stalks from  
800 diatom *Didymosphenia geminata* and their change due to adsorption of selected metal  
801 ions. *J Phycol.* 2017;53(4).
- 802 52. Chlanda A, Kijeńska-Gawrońska E, Zdunek J, Swieszkowski W. Internal  
803 nanocrystalline structure and stiffness alterations of electrospun polycaprolactone-  
804 based mats after six months of in vitro degradation. An atomic force microscopy assay.  
805 *J Mech Behav Biomed Mater* [Internet]. 2020 Jan;101(August 2019):103437.  
806 Available from: <https://linkinghub.elsevier.com/retrieve/pii/S1751616119305156>
- 807 53. Sader JE, Borgani R, Gibson CT, Haviland DB, Michael J, Kilpatrick JI, et al. A virtual  
808 instrument to standardise the calibration of atomic force microscope cantilevers. *Rev*  
809 *Sci Instrum* [Internet]. 2016 Sep 1;87(9):093711. Available from:  
810 <http://dx.doi.org/10.1063/1.4962866>
- 811 54. Wu KC, You HI. Determination of solid material elastic modulus and surface energy  
812 based on JKR contact model. *Appl Surf Sci.* 2007;253(20):8530–7.
- 813 55. Toolan DTW. Straightforward technique for in situ imaging of spin-coated thin films .  
814 *Opt Eng.* 2015;54(2):024109.
- 815 56. Toolan DTW, Howse JR. Development of in situ studies of spin coated polymer films.  
816 *J Mater Chem C.* 2013;1(4):603–16.
- 817 57. Mokarian-Tabari P, Geoghegan M, Howse JR, Heriot SY, Thompson RL, Jones RAL.  
818 Quantitative evaluation of evaporation rate during spin-coating of polymer blend films:  
819 Control of film structure through defined-atmosphere solvent-casting. *Eur Phys J E.*  
820 2010;33(4):283–9.
- 821 58. Heriot SY, Jones RAL. An interfacial instability in a transient wetting layer leads to  
822 lateral phase separation in thin spin-cast polymer-blend films. *Nat Mater.*  
823 2005;4(10):782–6.

- 824 59. Drelich JW, Boinovich L, Chibowski E, Volpe C Della, Hołysz L, Marmur A, et al.  
825 Contact Angles: History of Over 200 Years of Open Questions. *Surf Innov* [Internet].  
826 2019;(March):1–25. Available from:  
827 <https://www.icevirtuallibrary.com/doi/10.1680/jsuin.19.00007>
- 828 60. Koningsveld R, Staverman AJ. Liquid–liquid phase separation in multicomponent  
829 polymer solutions. I. Statement of the problem and description of methods of  
830 calculation. *J Polym Sci Part A-2 Polym Phys* [Internet]. 1968 Feb;6(2):305–23.  
831 Available from: <http://doi.wiley.com/10.1002/pol.1968.160060201>
- 832 61. Utracki LA, Wilkie CA. Polymer blends handbook. *Polymer Blends Handbook*. 2014.  
833 1–2378 p.
- 834 62. Ying Q, Chu B. Overlap concentration of macromolecules in solution. *Macromolecules*  
835 [Internet]. 1987 Mar;20(2):362–6. Available from:  
836 <https://pubs.acs.org/doi/abs/10.1021/ma00168a023>
- 837 63. Kim JK, Taki K, Nagamine S, Ohshima M. Periodic porous stripe patterning in a  
838 polymer blend film induced by phase separation during spin-casting. *Langmuir*.  
839 2008;24(16):8898–903.
- 840 64. Heier J, Kramer EJ, Groenewold J, Fredrickson GH. Kinetics of individual block  
841 copolymer island formation and disappearance near an absorbing boundary.  
842 *Macromolecules*. 2000;33(16):6060–7.
- 843 65. Coveney S, Clarke N. Pattern formation in polymer blend thin films: Surface  
844 roughening couples to phase separation. *Phys Rev Lett*. 2014;113(21):1–5.
- 845 66. Mecke K. Additivity, Convexity, and Beyond: Applications of Minkowski Functionals  
846 in Statistical Physics. *Stat Phys Spat Stat* [Internet]. 2000;111–84. Available from:  
847 [http://link.springer.com/chapter/10.1007/3-540-45043-2\\_6](http://link.springer.com/chapter/10.1007/3-540-45043-2_6)
- 848 67. Wolf BA. Improvement of polymer solubility: Influence of shear and of pressure. *Pure*

- 849 Appl Chem. 1997;69(5):929–33.
- 850 68. Du B, Tsui OKC, Zhang Q, He T. Study of Elastic Modulus and Yield Strength of  
851 Polymer Thin Films Using Atomic Force Microscopy. *Langmuir* [Internet]. 2001  
852 May;17(11):3286–91. Available from: <https://pubs.acs.org/doi/10.1021/la001434a>
- 853 69. Landel RF, Nielsen LE. *Mechanical properties of polymers and composites*. CRC  
854 press; 1993.
- 855 70. Torres JM, Stafford CM, Vogt BD. Impact of molecular mass on the elastic modulus of  
856 thin polystyrene films. *Polymer (Guildf)* [Internet]. 2010;51(18):4211–7. Available  
857 from: <http://dx.doi.org/10.1016/j.polymer.2010.07.003>
- 858 71. Kok CM, Rudin A. Prediction of Flory–Huggins interaction parameters from intrinsic  
859 viscosities. *J Appl Polym Sci*. 1982;27(2):353–62.
- 860 72. Lee SH, Lee SB. The Hildebrand solubility parameters, cohesive energy densities and  
861 internal energies of 1-alkyl-3-methylimidazolium-based room temperature ionic  
862 liquids. *Chem Commun*. 2005;(27):3469–71.
- 863 73. Bormashenko E, Malkin A, Musin A, Bormashenko Y, Whyman G, Litvak N, et al.  
864 Mesoscopic patterning in evaporated polymer solutions: Poly(ethylene glycol) and  
865 room-temperature-vulcanized polyorganosilanes/-siloxanes promote formation of  
866 honeycomb structures. *Macromol Chem Phys*. 2008;209(6):567–76.
- 867 74. Uchiyama H, Matsui T, Kozuka H. Spontaneous Pattern Formation Induced by  
868 Bénard–Marangoni Convection for Sol–Gel-Derived Titania Dip-Coating Films: Effect  
869 of Co-solvents with a High Surface Tension and Low Volatility. *Langmuir* [Internet].  
870 2015 Nov 17;31(45):12497–504. Available from:  
871 <https://pubs.acs.org/doi/10.1021/acs.langmuir.5b02929>  
872  
873